TRABAJO FIN DE MÁSTER

Máster en Física

CONTRIBUTION OF THE RADIATIVE HEAT TRANSFER MECHANISM TO THE TOTAL THERMAL CONDUCTIVITY OF ANISOTROPIC CELLULAR MATERIALS

Author: **Jorge Torre Ordás**

Tutor: **Miguel Ángel Rodríguez Pérez**

TABLE OF CONTENTS

CONTRIBUTION OF THE RADIATIVE HEAT TRANSFER MECHANISM TO THE TOTAL THERMAL CONDUCTIVITY OF ANISOTROPIC CELLULAR MATERIALS

Resumen

Con el fin de comprender y mejorar el comportamiento de los materiales celulares poliméricos como aislantes térmicos, este trabajo centra su estudio en la contribución del mecanismo de transferencia de calor por radiación en la conductividad térmica total de materiales celulares con diferentes coeficientes de anisotropía. El estudio comienza con una caracterización de los materiales seleccionados, materiales celulares en base poliestireno fabricados mediante un proceso de extrusión, en términos de su estructura celular y su conductividad térmica en función de la temperatura. Seguidamente, se determina la contribución radiativa para cada una de las tres direcciones principales de los materiales mediante tres metodologías independientes: espectroscopía de infrarrojos por transformada de Fourier (FTIR), derivación a partir de la conductividad total usando modelos teóricos, y derivación teórica a partir del modelo propuesto por Glicksman. Finalmente, se discuten los resultados obtenidos mediante las diferentes metodologías y se estudia el efecto de la anisotropía en el mecanismo de trasmisión del calor por radiación, estableciendo correlaciones con la estructura de los materiales.

Abstract

In order to understand and improve the performance of polymeric cellular materials as heat insulators, the contribution of the radiative transfer mechanism to the total thermal conductivity in cellular materials with different ratios of anisotropy is studied. Cellular materials based on polystyrene produced by an extrusion process are considered. The study begins with a characterization of the selected materials in terms of cellular structure and thermal conductivity as a function of temperature. Then, the radiative contribution for each of the three principal directions in the materials is obtained by three independent methodologies: Fourier Transform Infrared (FTIR) spectroscopy, derivation from the total conductivity using theoretical models, and theoretical calculation from the model proposed by Glicksman. Finally, the results yielded by these methodologies and their differences in the three principal directions are discussed, The effect of anisotropy on the radiative heat transfer mechanism is also analysed establishing correlations with the cellular structure.

Nomenclature

$E_{b,\lambda}$	black body spectral emissive power
E_b	black body total emissive power
f_s	fraction of mass in the struts
g	geometrical factor
K_R	Rosseland extinction coefficient
K_G	Glicksman extinction coefficient
K_w	solid polymer extinction coefficient
K_λ	spectral extinction coefficient
L	sample thickness
m	linear regression slope
n	real refractive index
R	anisotropy ratio
T	temperature
T_λ	transmittance
ϕ	mean cell size
$\mathbf{\Phi}$	energy flux
λ	wavelength
$\bar{\bar{\lambda}}_c$	convection tensor
$\bar{\bar{\lambda}}_g$	gas conduction tensor
$\bar{\bar{\lambda}}_r$	radiative transfer tensor
$\bar{\bar{\lambda}}_s$	solid conduction tensor
$\bar{\bar{\lambda}}_T$	total conductivity tensor
λ_c	convection contribution
λ_g	gas conduction contribution
λ_r	radiative transfer contribution
λ_s	solid conduction contribution
λ_T	total conductivity
λ_{air}	air total conductivity
λ_{solid}	solid polymer total conductivity
ρ_r	relative density
σ	Stephan-Boltzmann-constant

Superscripts

$\square^i$	i direction

1. Introduction

Households are responsible for a significant share of the global energy consumption. Indeed, the building sector is the second most consuming sector in the European Union (EU) (27%) only surpassed by transportation (31%) [1]. One of the most acknowledged means of reducing the amount of energy used in households is by enhancing its efficiency with the use of improved thermal insulators [2, 3].

Cellular materials are two-phase composites in which the gas phase has been dispersed in a continuous or discontinuous solid phase [4]. Particularly, polymeric cellular materials are well known for their capability to present low thermal conductivities, low density, low cost and ease of production and installation. Some of the most common materials used nowadays are extruded polystyrene (XPS), expanded polystyrene (EPS) and rigid polyurethane foams (RPU) [5]. Hence, understanding and improving their performance as heat insulators is beneficial for both environmental and economical points of view.

Among the very different types of polymeric cellular materials, closed cell foams are the ones with the lowest thermal conductivity, since they own low volume fraction of solid phase, low conductivity of the enclosed gas [6, 7], and, when the cell size is small, negligible convection (see section 2). A common way authors have approached the problem of understanding the thermal conductivity is taking into account the four mechanisms of heat transfer: conduction through the solid phase, conduction through the gas phase, convection and radiation [8-13]. In low density cellular materials, this last term can reach up to 40% of the total thermal conductivity [14-16]. That is the main reason why several authors have previously studied this topic. For instance, Glicksman

et al. [17], Williams and Aldao [18], and Kuhn et al. [19] focused on the theoretical prediction of the radiative heat transfer of different types of polymeric cellular materials. Other authors such as Heinemann and Caps [20], Tseng and Kuo [21] or, more recently Arduini et al. [11] showed an experimental approach to measure the extinction coefficient, a key parameter in the radiative contribution.

Most cellular polymers are anisotropic. Due to the production process the cells are not isotropic and, in fact, they can be oriented in a given direction as shown in Figure **1** [22]. In the case of extrusion, which is a continuous process in which the blowing agent is introduced in the polymer melt that is extruded through a flat die to produce a foamed sheet (see Figure **2**) [4], it is common to produce cellular structures with a clear directionality. In fact, extrusion is a directional process in which we can distinguish between the machine direction (MD), the traverse direction (TD) and the thickness direction (Z) [5]. Therefore, the materials can be characterized by a certain degree of anisotropy associated with different cell sizes in three orthogonal directions. It is expected that this characteristic anisotropy could have an influence on the radiative heat transfer in each direction.

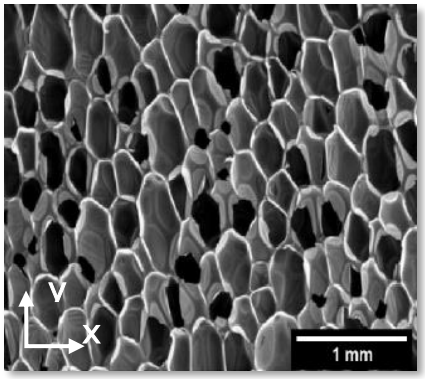

Figure 1. Example of an anisotropic cellular material: the majority of the cells have a larger size in the one direction (in this case, the y direction).

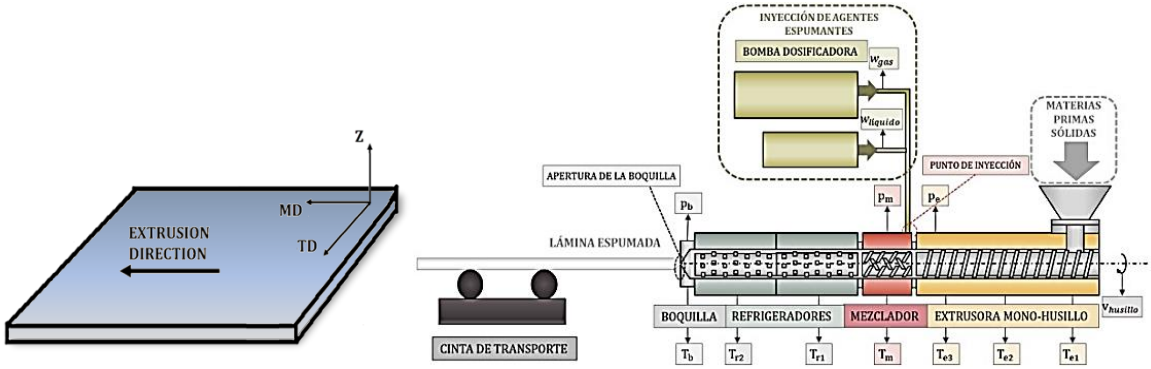

Figure 2. Diagram of the extrusion process machinery and assignment of principal directions of the resulting material: machine direction (MD), transverse direction (TD) and thickness direction (Z).

Despite the numerous works in the literature on the analysis of the radiative contribution, none has been found in which the effect of the anisotropy of the cellular structure of cellular materials on the radiative transfer is studied thoroughly. Hence, this

research work aims to cover this gap analysing the radiation contribution in three orthogonal directions for different extruded polystyrene foams with a variety of ratios of anisotropy and using different methods.

2. Theoretical background

Fourier's law of heat transfer states that the energy flux $\boldsymbol{\Phi}$ (i.e., heat energy per unit time and cross-sectional area) passing through a homogeneous volume is proportional to, and in the direction of, the negative temperature gradient between both sides (see Equation (1)):

$$\boldsymbol{\Phi} = -\bar{\bar{\lambda}}_T \boldsymbol{\nabla} T, \tag{1}$$

being $\bar{\bar{\lambda}}_T$ the proportionality second-order tensor for anisotropic materials. The homogeneity assumption is a good approximation as long as the pore size is sufficiently small compared to the external dimensions of the materials [16]. Given that cellular materials can be considered as orthotropic materials- this is, they present symmetry under orthogonal transformations-, in the correct orthogonal basis, $\bar{\bar{\lambda}}_T$ can be written as [23, 24]:

$$\bar{\bar{\lambda}}_T = \begin{pmatrix} \lambda_T^{xx} & 0 & 0 \\ 0 & \lambda_T^{yy} & 0 \\ 0 & 0 & \lambda_T^{zz} \end{pmatrix}, \tag{2}$$

where each λ_T^{ii}, $i = x, y, z$, is the total thermal conductivity in the i direction. In the cellular materials terminology, it is common to use the orthogonal directions MD, TD and Z, where, MD represents the machine direction of the extrusion process, TD the transverse one, and Z the perpendicular to both [25], as shown in Figure 2.

In the case of polymeric cellular materials, the heat transfer process can be broken down into four contributions as shown in Equation (3): conduction through the solid phase $\bar{\bar{\lambda}}_s$, conduction through the gaseous phase $\bar{\bar{\lambda}}_g$, radiation transmission $\bar{\bar{\lambda}}_r$, and heat convection $\bar{\bar{\lambda}}_c$ [8-13]. This is typically an accurate approximation which considers independence between all heat transfer mechanisms [6, 8].

$$\bar{\bar{\lambda}}_T = \bar{\bar{\lambda}}_s + \bar{\bar{\lambda}}_g + \bar{\bar{\lambda}}_r + \bar{\bar{\lambda}}_c \tag{3}$$

While the convection term can be neglected for cellular materials with cell sizes under 4 mm, and in fact, it will be neglected here, the other ones cannot [5, 8, 26].

Considering from now on the conductivities in only one direction and removing the superscript for the sake of notation simplicity, each term in Equation (3) can be modelled as follows [5, 8, 16]:

- *Conduction through the solid phase* λ_s.

This contribution accounts for about $10-15\%$ of the total conductivity in typical XPS foams [3]. The solid polymer in a cellular material takes the form of cell walls and struts as can be seen in Figure **3.a**. Therefore, heat moves in non-linear paths. An approximated model proposed by Glicksman [8] can be used to predict the contribution of conduction through the solid as shown in Equation (4). The model considers that the contribution in the foam is the one in the solid multiplied by the volume fraction of solid or relative density ρ_r in the material and a geometrical correction factor.

$$\lambda_s^i = g\rho_r\lambda_{solid} = \left(\frac{1}{3}f_s\sqrt{R^i} + \frac{2}{3}(1-f_s)\sqrt[4]{R^i}\right)\rho_r\lambda_{solid}\,, \tag{4}$$

$$R^i = \frac{2\phi^i}{\phi^j + \phi^k} \tag{5}$$

In Equation (4), g is the geometrical factor of the material, which can be expressed in terms of the fraction of mass in the struts f_s and the anisotropy ratio in the i direction R^i. The cells in low density cellular polymers are polyhedral, being the solid phase distributed in the walls, edges, and vertex of this polyhedral. The parameter f_s can be defined as the ratio between the amount of solid polymer located in the struts (edges & vertex) and the amount located in the sum of walls and struts (see Figure **3.b**). On the other hand, the parameter R^i is computed (Equation (5)) as the ratio between the mean value of the cell size in the i direction ϕ^i, and the mean value of the cell sizes in the two perpendicular directions (j and k), being the mean cell size in a given direction the average of all lengths of the cells in that direction. Also, in Equation (4), ρ_r is the relative density of the foam, which is computed as the ratio of the density of the foam over the one of the solid polymer. This parameter is, to a good approximation, the volume fraction of solid in the foam [27]. Finally, λ_{solid} is the total conductivity of the solid polymer.

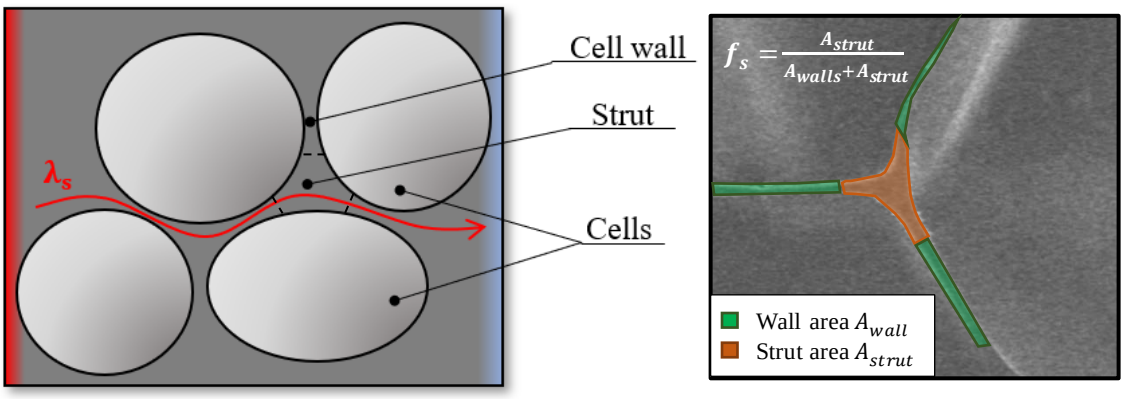

(a) (b)

Figure 3.a) Schematic visualization of the heat moving through the solid phase of a foam. **b)** Definition of the mass fraction in the struts f_s.

- *Conduction through the gas phase λ_g.*

This mechanism is the most contributing one, typically accounting for about 60 to 70% of the total conductivity [3]. The contribution of the gas enclosed by cells can be modelled multiplying the conductivity of the gas, which is air for the foams under study λ_{air}, by the volume fraction of air (or porosity) of the foam [8]:

$$\lambda_g = \lambda_{air}(1 - \rho_r) \tag{6}$$

- *Radiative transfer* λ_r.

This term can be responsible for about 10 to 40% of the total conductivity [3, 14, 15]. For samples with enough thickness, the radiation process can be analysed as a diffusion process (diffusion approximation). Under the hypothesis that the scattering is isotropic and the radiation's mean free path is much shorter than the foam thickness, the Rosseland equation states that the radiative contribution can be written as [8]:

$$\lambda_r = \frac{16n^2\sigma T^3}{3K_R}, \tag{7}$$

where σ is the Stefan-Boltzmann constant, T is the material temperature, n is its refractive index (approximately 1 for low density cellular materials[7]) and K_R is the Rosseland extinction coefficient obtained as shown further in this document. As it can be seen from Equation (7), the Rosseland extinction coefficient is an essential parameter for the calculation of the radiative contribution.

Glicksman *et al.*[8] proposed a theoretical method to compute this extinction coefficient K_R for polyurethane closed-cell foams. They considered an isotropic porous media with regular pentagonal dodecahedral cells, which is very close to reality in many different foams [16], and randomly oriented blackbody struts. For the struts contribution, they considered that its cross-sectional area was constant and it occupied two-thirds of the area of an equilateral triangle. For the walls contribution, they assumed thin enough cell walls (optically thin limit). The expression for the extinction coefficient proposed by these scientists (K_G) can be seen in Equation (8):

$$K_G = K_{edges} + K_H K_w = 4.10\frac{\sqrt{f_s\rho_r}}{\phi} + (1 - f_s)\rho_r K_w\,, \tag{8}$$

where ϕ is the mean cell size of the cellular polymer and K_w is the extinction coefficient of the solid polymer.

During this research project, K_R will be obtained by two additional methods, that will be explained in the next section.

3. Experimental procedure

3.1 Materials

Two sets of polymeric cellular materials were selected for this study as can be seen in Table **1**. The first set is composed of two extruded polystyrene (XPS) foams of big dimensions ($30 \times 30 \times 7.5\ cm$), which are characterized by high anisotropy ratios, whereas the second one is composed of six XPS foams of smaller dimensions ($15 \times 15 \times 5\ cm$) and lower densities than the first set, but similar between each other, and a variety of cell sizes. The samples in the first and second set were kindly donated by the industrial companies ISOFOAM (Kuwait) (BXPS samples) and URSA Ibérica (YXPS samples) respectively. All of them were produced by an extrusion process (see Figure **2**) of amorphous polystyrene, using CO_2 and $EtOH$ as foaming agents, talc as nucleation agent, and a polymeric flame retardant based on bromine. A few weeks after production, it is known that the gases used as blowing agents diffuse out of the foam and air diffuses into the cells. As our study was conducted several months after the foams production, it is possible to consider that air is inside the cells of all the cellular polymers under study [3].

Table 1. Description of the selected samples.

Set	Sample name	Relative density ρ_r	Colour
1st	BXPS1	0.033	Blue
	BXPS2	0.046	(B)
2nd	YXPS0	0.027	Yellow (Y)
	YXPS1	0.028	
	YXPS2	0.026	
	YXPS3	0.027	
	YXPS4	0.027	
	YXPS5	0.028	

3.2 Material characterization

- ***Density***

In order to obtain the relative density ρ_r, the density of the solid polymer, ρ_s was considered to be the acknowledged value of $1050\ kg/m^3$ [15, 28]. The foams density was measured in two ways in the laboratory: for the samples in the first set, which were bigger, the geometrical method was used for the entire $30 \times 30 \times 7.5\ cm$ samples. This method consists in accurately measuring the volume and the mass of the material using a calliper and a precision balance respectively, and performing their quotient. The error of this measurements is 1.5%. For the samples in the second set, which were smaller, the Archimedes principle was used. This method is based on measuring the buoyant force caused by the immersed sample in a liquid of know density. This force, using the Arquimedes principle, is equivalent to the weight of the fluid displaced by the sample [29]. For these measurements the kit for density determination of an AT261 balance from Mettler was used. The dimensions of the samples in this case where approximately $1 \times 1 \times 1\ cm$. The error in this type of measurement is 5%.

- ***Cellular structure parameters***

Parameters such as cell size or anisotropy ratio were measured using AutoCell [30], a Fiji (ImageJ) [31] macro designed to automatically analyse several micrographs of a foam that has been previously prepared with paint, in order to outline the cell walls for the programme to be able to distinguish them. When an image is given to AutoCell, it binarizes it and segments the cells. Afterwards, it measures all cell sizes and performs calculations with them (Figure **4**). The error in this measurement is 4%. With this approach, the cell size in each direction can be obtained and, then, the anisotropy ratios can be calculated using Equation (5).

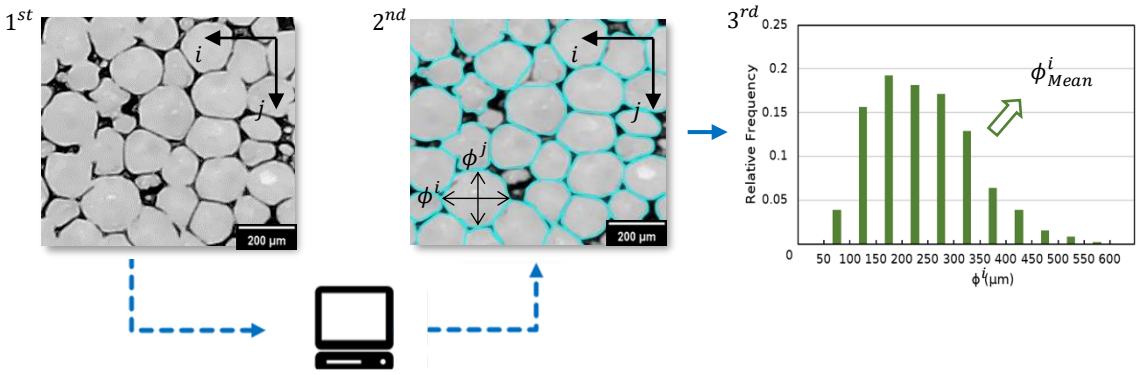

Figure 4. Diagram of the basic functioning of AutoCell. 1^{st}: Micrograph of the painted foam. 2^{nd}: Cells segmentation and calculation of all cell sizes in the directions i and j. 3^{rd}: Obtainment of the material parameters such as the mean cell size.

Another key parameter, which is the fraction of mass in the struts, f_s, was measured for the materials in the first set of Table **1** using X-ray tomography with the methodology developed by S. Pérez-Tamarit *et al.* [32]. This technique consists in using image analysis with a set of images obtained by X-ray tomography. With ImageJ, a thickness distribution graph (or histogram) can be computed by analysing the amount of solid phase pixels in the three dimensions (length, width and depth with the next and previous images) that surround each of the pixels of the micrograph. After that, a deconvolution of the main curve can be carried out, separating between the contributions of the walls (with smaller thickness) and the struts (with larger thickness). Then, the parameter f_s is the ratio between the area below the struts curve and the sum of the areas of struts and walls.

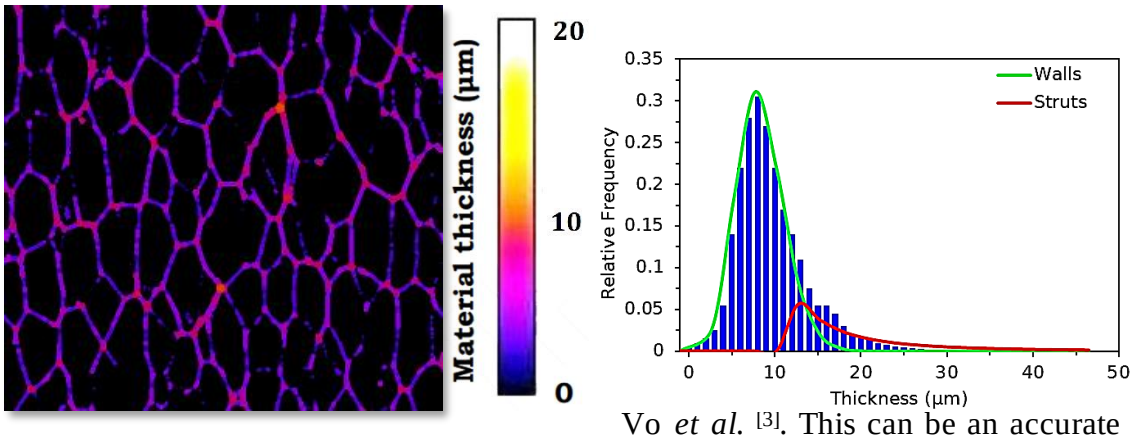

Vo *et al.* [3]. This can be an accurate value of f_s given that the only variable parameter is the cell size and the typical values of f_s for these types of foams usually range between 0.1 and 0.25 [3].

- ***Radiative contribution λ_r.***

For all samples, the parameter λ_r was obtained using three different methodologies, which are described below:

I) FTIR spectroscopy method.

In order to obtain the Rosseland extinction coefficient K_R in Equation (7), transmittance measurements were carried out.

For this, several samples of thicknesses in the range of $0.8 - 6.3\ cm$ were cut for the three principal directions for each foam in Table **1**. The samples' thickness (L), was precisely measured using a DMA7 device from PerkinElmer. It consists of two parallel plates, one of which is stationary, and the other one presses the sample with a force of $10\ mN$, which is too low to deform the foam. The separation between the plates is measured once the moving plate finds the sample with an accuracy of 0.1 microns.

After that, the samples were subjected to transmission FTIR spectroscopy in a Bruker Tensor 27 with a LN-MCT Mid 2x2mm detector. The experiment was conducted in the interval of wavenumbers from 4000 to 600 cm^{-1} with a resolution of $2\ cm^{-1}$. Hence, a total of 3562 data points were collected. This interval of wavenumbers is of high relevance as the structural information on the target matter is mostly readily available from its mid-infrared spectrum [33]. In addition, the values of the number of scans, the aperture setting, the phase resolution and the correction noise were 32, $6\ mm$, 8 and 25 points respectively.

Once the transmittance was obtained, a methodology similar to the one proposed by R. A. Campo *et al.* [7] was used to compute K_R. According to Beer's law, the spectral extinction coefficient K_λ for homogeneous samples in which radiation extinction remains constant along the thickness can be obtained as it follows [34]:

$$T_\lambda = \exp\left(-\int_0^L K_\lambda\, dx\right) \rightarrow \quad K_\lambda = -\frac{\ln(T_\lambda)}{L}, \tag{9}$$

where T_λ is the transmittance and L is the sample's thickness. Therefore, the spectral extinction coefficient can be obtained with a linear regression of the dependency of $\ln(T_\lambda)$ with L.

Once K_λ is obtained, the Rosseland extinction coefficient can be computed as it follows [34, 35]:

$$\frac{1}{K_R} = \frac{\int_0^\infty \frac{1}{K_\lambda}\frac{\partial E_{b,\lambda}}{\partial T}\, d\lambda}{\int_0^\infty \frac{\partial E_{b,\lambda}}{\partial T}\, d\lambda} = \int_0^\infty \frac{1}{K_\lambda}\frac{\partial E_{b,\lambda}}{\partial E_b} d\lambda\,, \tag{10}$$

where $E_{b,\lambda}$ is the black body hemispherical emissive power and E_b is the black body total emissive power. This integral was solved analytically for the purposes of this work. An error of 10% was estimated for the values obtained.

II) Method of subtraction of contributions from the total conductivity.

The radiative contribution λ_r can be obtained by means of subtracting the λ_s and λ_g terms from the total conductivity in Equation (3). For this, the total conductivity λ_T was measured in two different ways depending on the set of samples in Table **1**. For the first set, there was enough amount of material to be able to cut the samples in big enough dimensions (see Figure **6**). For this reason, in this case, a steady heat flow conductivity meter Laser Comp FOX314 was used in agreement with the ASTM C518 method [36]. This conductivity meter is provided with a $10 \times 10\ cm$ sensor in a $30 \times 30\ cm$ cavity. Therefore, the samples could fit in covering the whole sensor. In order to measure the total conductivity in the three main directions, a specific arrangement of the samples was used (Figure **6**). For the study of each of the directions MD and TD, four pieces of the main material sheet were cut, rotated and put together next to each other. The chosen mean temperatures between the plates were $10, 20, 25, 30$ and $40\ ºC$. This was done setting a difference in the temperature of each plate of ΔT of $20ºC$. The precision of this measurements was 2%.

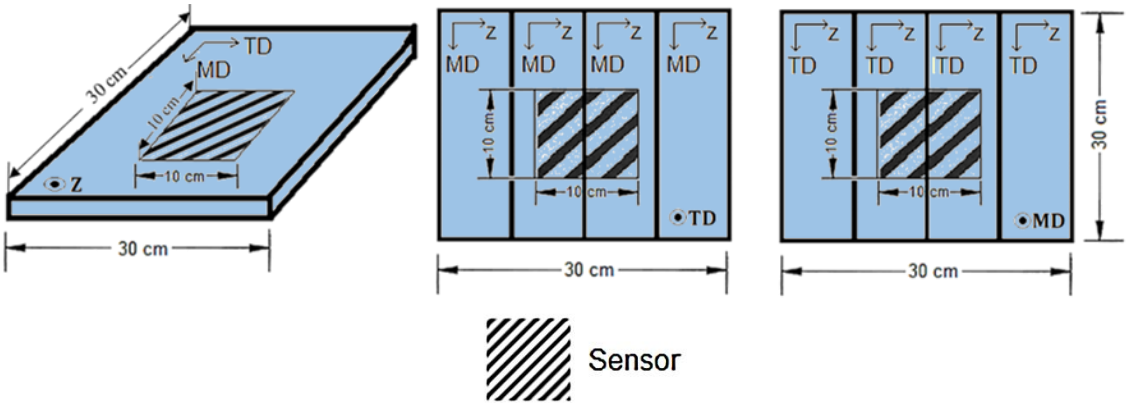

Figure 6. Dimensions and disposal of the samples and heat flow sensor used for measuring the thermal conductivity in different directions of the first set of samples in Table **1**.

For the second set, given that there was not enough amount of material to cover the whole sensor surface of heat flow conductivity meter Laser Comp FOX314, three samples were cut out of all the materials- one for each principal direction- with dimensions of $2 \times 2 \times 1.5\ cm$ approximately, as shown in Figure **7**. In order to obtain λ_T, two small external $1 \times 1\ cm$ heat flow sensors gSKIN® XP-27 9C, from GreenTEG AG were used, one above and one below the samples. Also, the temperature was measure using a gSKIN® DLOG-4219 data logger cable, from GreenTEG AG. Then, the whole assembly was introduced into the Laser Comp FOX314 covered with EVA sheets to eliminate convection simulating the arrangement used for the first set and in order to set the desired temperatures for the upper and lower plates in contact with the samples (see Figure **8**). The same temperatures as in the first set was chosen. In this case, the data coming from the Laser Comp was ignored and the one coming from the smaller sensors were used. The precision of this measurements was 3%.

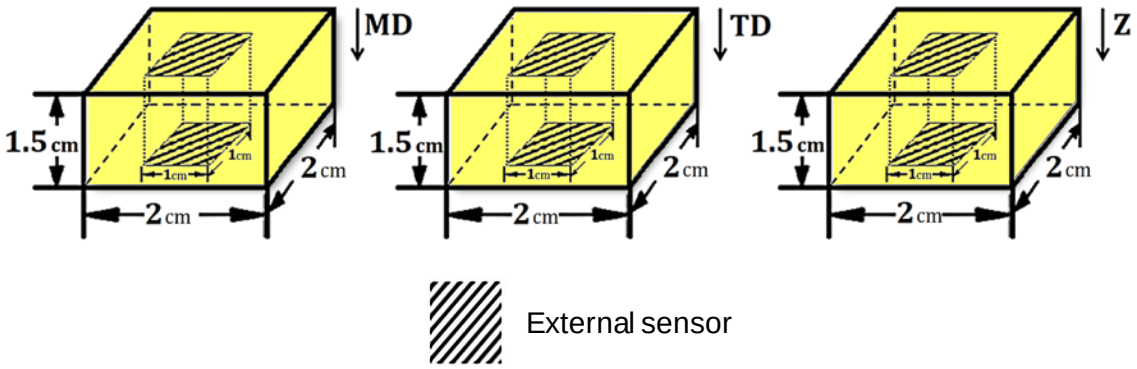

Figure 7. Dimensions of the samples and heat flow sensor used for the total conductivity characterization of all samples included in the second set of Table **1**.

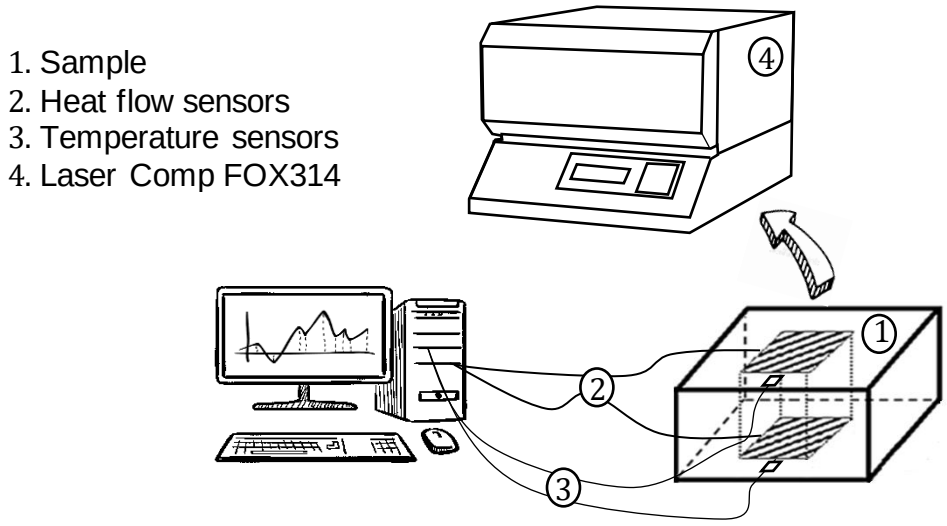

Figure 8. Experimental set-up of the total conductivity measurements for the second set of materials. The sample is introduced in the Laser Comp and covered with EVA sheets in order to eliminate air currents inside.

Once the total conductivity λ_T was obtained for all materials and for each of the three directions, the radiative contribution λ_r was obtained subtracting the λ_s and λ_g terms considering the theoretical equations(3), (4) and (6), in which the experimental values of f_s, R and ρ_r are used. For λ_{solid} and λ_{air}, their dependence with temperature was taken into account (Table **2**). In the case of λ_{solid}, twelve stacked sheets of $20 \times 20\ cm\ x\ ...\ cm$ of solid polystyrene were placed in the heat flow meter FOX314 at the same temperature intervals as the cellular materials. For λ_{air}, the temperature dependence was taken from the literature [37]. Finally, in order to obtain the Rosseland extinction coefficient K_R, a linear regression of the λ_r contribution with cubic temperature was performed using Equation (7). A visual example of this procedure can be found in Figure **9**.

Table 2. Dependence of the thermal conductivities of the solid PS and air with temperature.

$T\ (ºC)$	10	20	25	30	40
$\lambda_{solid}\ (mW\ /\ m\ K)$	140.7	142.5	143.7	144.9	147.3
$\lambda_{air}\ (mW\ /\ m\ K)$	25.1	25.9	26.2	26.6	27.3

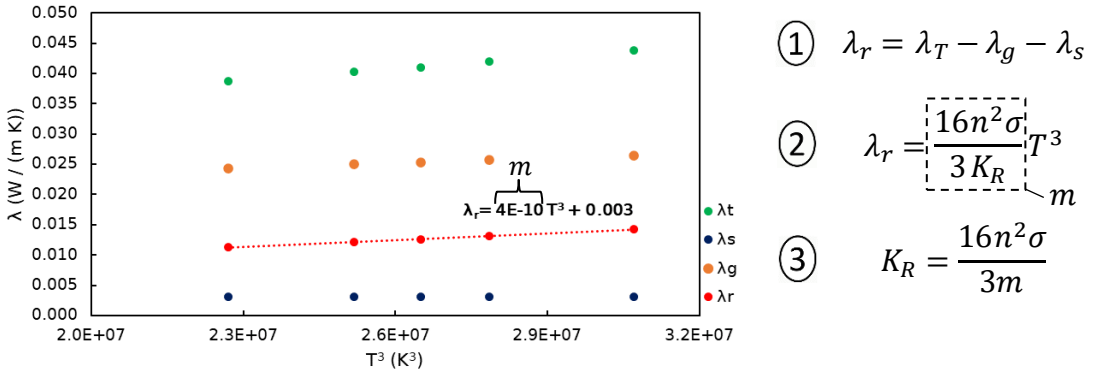

Figure 9. Rosseland extinction coefficient compute breakdown from the radiative contribution λ_r using the experimental data of the total conductivity and the theoretical models for the contributions λ_s and λ_g.

III) Glicksman's model method.

For this last method, Equation (8) was used to calculate the Rosseland extinction coefficient with the experimental values of f_s, ρ_r, and ϕ in each direction. Regarding K_w, it was considered to be the Rosseland extinction coefficient of the solid polystyrene, which was obtained with the FTIR spectroscopy method for a thin polystyrene (PS) film leading to a value of $43.1 \pm 4.3\ cm^{-1}$.

4. Results and discussion

4.1 First set of materials.

This section of the document discusses the results for the first set of samples in Table **1**, which are suitable for a discussion about the effects of anisotropy on the heat transfer by radiation.

- ***Structural characterization.***

In order to carry out a study on the effects of anisotropy, focus has to be given to parameters such as cell size and anisotropy ratio. The results of these two magnitudes for the first set of materials are shown in Table **3**. As it can be seen, the selected foams have a considerable anisotropic character. A visual example of this is bottom image in Figure **10**, where the anisotropy is clearly observable, given that the majority of cells are oriented towards the Z direction in the MD-Z plane.

Table 3. Results of the main cellular structural parameters of the materials in the first set.

Sample	f_S	$\phi^{TD}(\mu m)$	$\phi^{MD}(\mu m)$	R^Z	R^{TD}	R^{MD}
BXPS1	0.186	292	212	1.38	1.04	0.66
BXPS2	0.183	177	117	1.34	1.12	0.63

The cells follow the same trend in both materials: $\phi^Z > \phi^{TD} > \phi^{MD}$, being the difference between the mean cell size in Z and MD very large. The anisotropy ratio in the Z direction reaches a very high value of 1.38 for the sample BXPS1 and 1.34 for the sample BXPS2. Conversely, the anisotropy in the MD direction reaches a low value of 0.66 for the sample BXPS1 and 0.63 for the sample BXPS2. The results show that the cells are clearly larger in the sample with lower density (BXPS1).

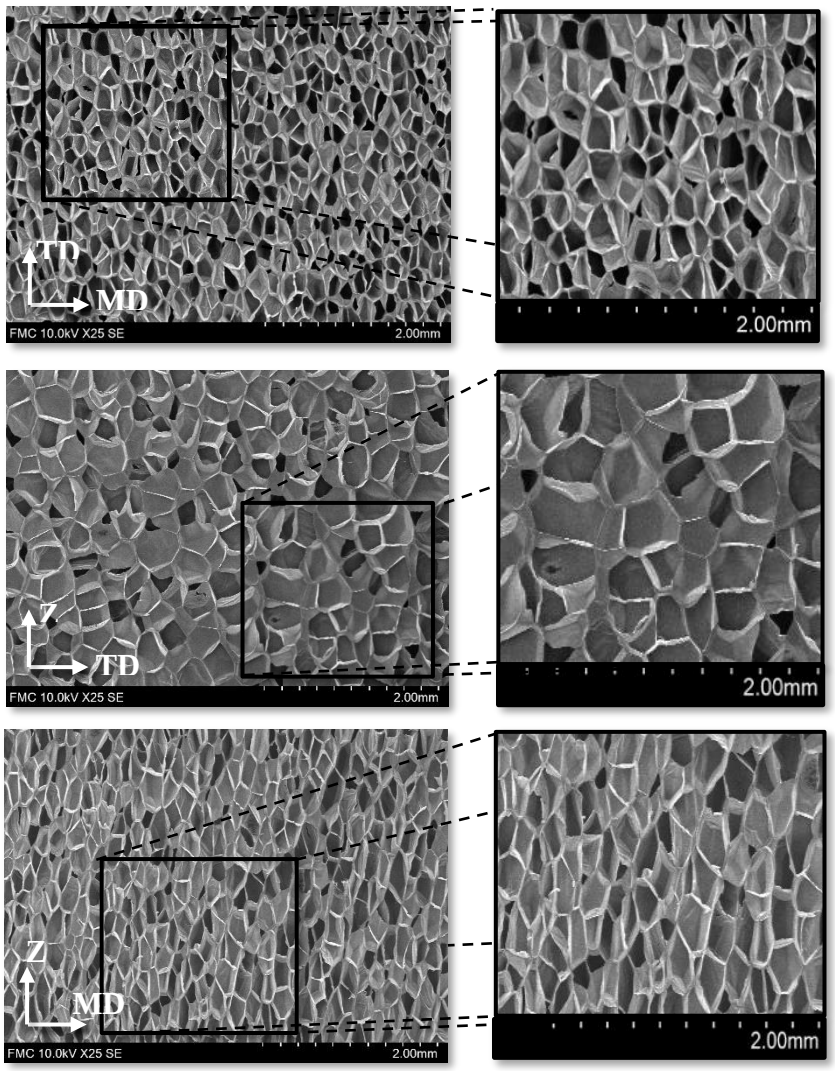

Figure 10. SEM micrographs of the three orthogonal cross-sectional areas of BXPS1.

In addition, the results of the fraction of mass in the struts f_s for both materials are shown in Figure **11**, where the total observed distribution of thicknesses of walls and struts is observed, as well as the deconvolution of each one. Although the cellular structure and density for these two materials is different, the distribution of mass in

struts and walls is similar. This is the expected result for XPS foams, in which the mass is mainly concentrated in the walls, and, therefore, the values of f_s are typically below 0.2 [3].

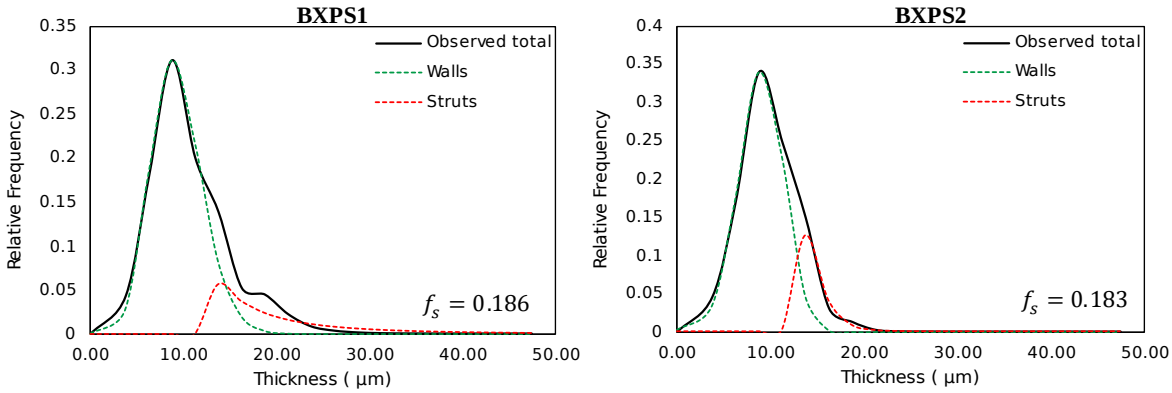

Figure 11. Observed total thicknesses distribution of walls and struts for the two materials in the first set of Table **1**. The dotted lines represent the deconvoluted peaks of distribution of walls and struts separately. The fraction of material in the struts for both materials is close to 0.18, which means that 82% of the mass is located in the cell walls and only 18% of the mass is located in the struts.

- ***Thermal characterization.***

The results of the total conductivities in the three directions MD, TD and Z for the first set of materials in Table **1** are given in Figure **12**. For both materials and all directions, the thermal conductivity increases with temperature. It can be observed that there are noticeable differences in the total conductivities between the three principal directions. In fact, changing the orientation from Z to TD can account for about $3-4\ mW/(m\cdot K)$ in the BXPS1 foam and about $2.5-4\ mW/(m\cdot K)$ in the BXPS2 foam, while changing from the Z to the MD direction, can do it for about $7-10\ mW/(m\cdot K)$ in the BXPS1 foam and about $6-8\ mW/(m\cdot K)$ in the BXPS2 foam. These differences mainly come from the radiative contribution, as the solid and gas conduction do not depend on cell size [16], something that will also be proved further in the document. Also, it is interesting to see that the total conductivity of the BXPS2 sample is, for each individual temperature and direction, lower than the one of BXPS1. This is due to its higher relative density and lower cell size.

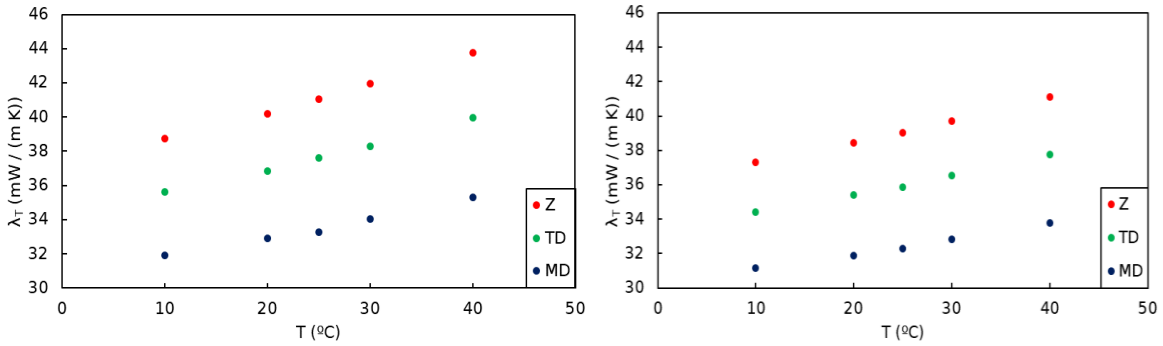

Figure 12. Dependence of the total conductivity of the BXPS1 (left) and BXPS2 (right) as a function of the temperature and for the different planes analysed.

- ***Extinction coefficient.***

The results of the Rosseland extinction coefficient obtained by the three methodologies outlined in section 3.2 are shown here.

I) FTIR spectroscopy method.

Figure **13** shows an example of a spectrogram obtained for the various thicknesses of the BXPS1 sample. Using a linear regression with Equation (9), an array of K_λ arises as in the example of Figure **14**. As it can be seen from Figure **14**, there exist nonzero extinction coefficients outside the absorbing bands. These are due to the Mie scattering phenomena in the walls and struts' boundaries, which grow in number as thickness increases. Because of the lack of an integrating sphere, almost all scattered radiation is lost, given that the detector subtends a solid angle of $0.51\ sr$, which is, approximately, a 4% of the total solid angle. This results in a higher Rosseland extinction coefficient in comparison with other methods as will be shown below.

The values of the Roseland extinction coefficient in different planes obtained by the FTIR spectroscopy method are listed in Table **4**. As it can be directly seen, there are clear differences in the extinction coefficient between directions due to the anisotropic character of the cell size. The tendency $K^{MD} > K^{TD} > K^{Z}$ is observed in both materials and this is directly relatable to the fact that $\phi^{Z} > \phi^{TD} > \phi^{MD}$. In those directions in which the cell size is larger, the radiation finds less cell walls and struts in its path and, therefore, has a larger mean free path.

A separation between the scattering and the absorption contribution to K_R was also possible by means of a base line fitting. The base line of each spectrum was calculated assigning the same constant value of transmittance to every wavenumber, making sure it describes the non-absorbing regions as optimally as possible. The results of these two contributions are in accordance with the expected: the absorption contribution has a low decreasing dependence with the increase in cell size because of the stretching of cell walls and the lower number of cells per unit length, whereas the scattering contribution feels a much larger dependence because of the lower number of scattering points as the number of cells per unit length decreases. It is also observable that the absorption contribution in the BXPS2 material is significantly larger than in BXPS1. This is

directly relatable with the fact that the BXPS2 material's density is higher with respect to the other: if there are more molecules in one material with respect to the other in the same volume of space, more absorption takes place.

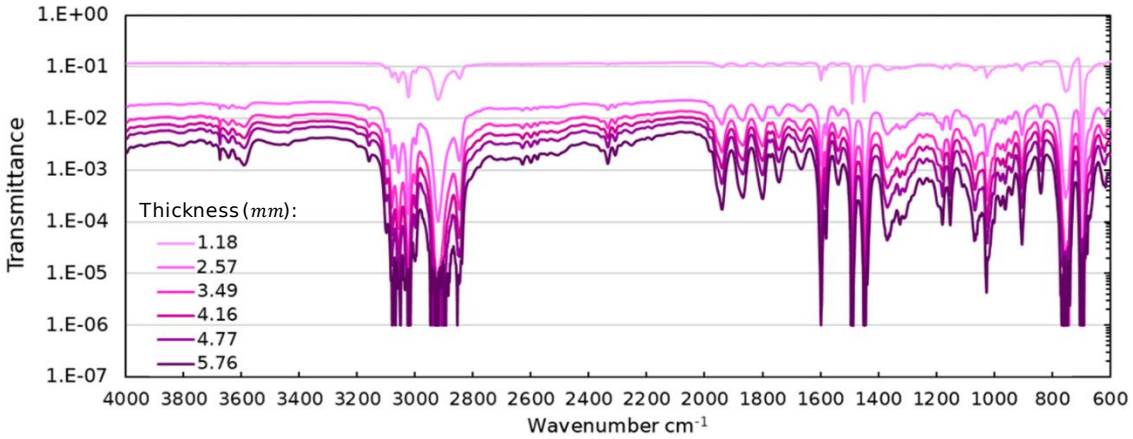

Figure 13. Transmittance spectra of several BXPS1 samples of different thicknesses with the infrared radiation passing through the Z direction.

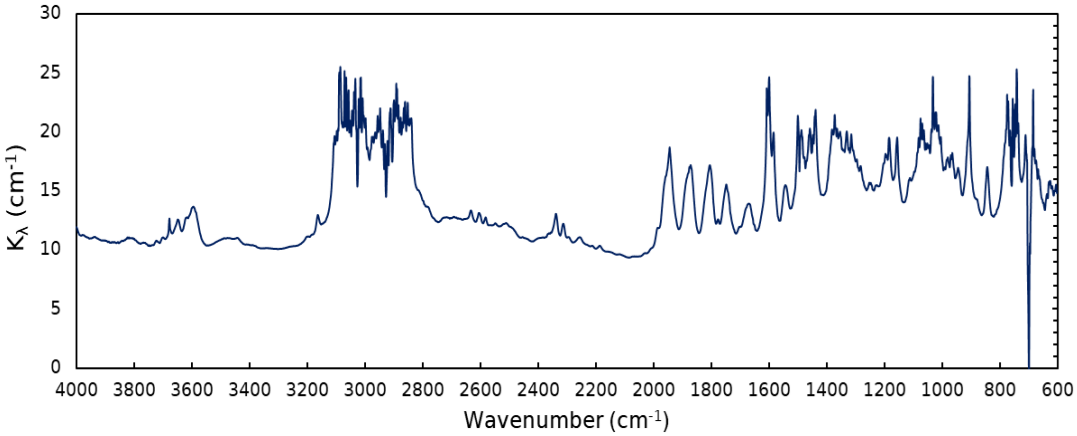

Figure 14. Spectral extinction coefficient K_λ for a BXPS1 set of samples when the infrared radiation is passing through the Z direction.

Table 4. Results of K_R for the first set of materials in Table **1** with the FTIR method.

FTIR Spectroscopy --- K_R (cm^{-1})					
Sample	**Direction**	ϕ (μm)	**Total**	**Scattering**	**Absorption**
BXPS1	**MD**	212	19.8	13.5	6.31
	TD	292	15.4	9.49	5.87
	Z	348	13.8	8.35	5.41
BXPS2	**MD**	117	20.2	11.1	9.06
	TD	177	16.6	7.68	8.94
	Z	197	14.7	5.82	8.84

A study on how much does K_R increase when the cell size ϕ reduces can be carried out by means of a linear regression of the ratios between those magnitudes (see Figure **16**). It is found that the ratio between extinction coefficients follows a linear relation with the inverse ratio of cell size as shown in Equation (11).

$$\frac{K_R^i}{K_R^j} = A\frac{\phi^j}{\phi^i} + B, \qquad A = 0.5, \;\; B = 0.6 \tag{11}$$

Interestingly, this means that orienting the material towards a direction with half the cell size will increase K_R an amount of 1.6 times the previous value.

II) Method of subtraction of contributions from the total conductivity.

The results of the Rosseland extinction coefficient yielded by this method are shown in Table **5**. Again, a similar tendency to the one obtained by the FTIR spectroscopy is found. This is $K^{MD} > K^{TD} > K^{Z}$. Interestingly, similar results of this magnitude are found for both materials BXPS1 and BXPS2, even though a slight increase should be expected for BXP2, given that it has lower total conductivity λ_T and higher relative density ρ_r, which greatly diminishes the gas phase contribution λ_g, being this one the one that affects the most.

Table 5. Results of K_R for the first set of materials with the subtraction method.

Subtraction method --- K_R (cm^{-1})			
Sample	**Direction**	ϕ (μm)	**Total**
BXPS1	MD	212	18.9
	TD	292	11.8
	Z	348	8.3
BXPS2	MD	117	20.8
	TD	177	11.6
	Z	197	8.10

In this case, a quadratic relation is found between the ratio of extinction coefficients and cell sizes. Indeed, this relation can be obtained if a quadratic regression is performed:

$$\frac{K_R^i}{K_R^j} = A\left(\frac{\phi^j}{\phi^i}\right)^2 + B\frac{\phi^j}{\phi^i} + C \;\rightarrow\; A = 4.9, \;\; B = 12.0, \;\; C = 8.7 \tag{12}$$

III) Glicksman's model method.

In this section, the results obtained applying the theoretical model proposed by Glicksman are studied. Table **6** shows the Rosseland extinction coefficient calculated by this method. Again, the same tendency is observed: the lower the cell size in any given direction, the greater the Rosseland extinction coefficient is. Here, the Glicksman model predicts a significantly higher value of K_R for the BXPS2 foam. Looking at Equation (8), one can see that this is caused by the increase in relative density and the decrease in cell size with respect to BXPS1.

It is remarkable that the ratio of Rosseland extinction coefficients of two directions is, in this case, proportional to the inverse ratio of cell sizes, as shown in Equation (13).

$$\frac{K_R^i}{K_R^j} = C\frac{\phi^j}{\phi^i}, \qquad C = 0.9 \tag{13}$$

This means that changing to a direction with half the cell size will increase the extinction coefficient a proportion of 1.8 times.

Table 6. Results of K_R for the first set of materials with the Glicksman's method.

Glicksman's method --- K_R (cm^{-1})			
Sample	**Direction**	ϕ (μm)	**Total**
BXPS1	MD	212	16.3
	TD	292	12.2
	Z	348	10.5
BXPS2	MD	117	34.0
	TD	177	23.1
	Z	197	20.9

- ***Comparison between the three methods.***

Once the results of all methods have been displayed, it is interesting to discuss whether the methods used were reliable and similar between each other. In Figure **15**, one can see that, in both materials, the results of all three methods are similar, except from the Glicksman model, in the case of BXPS2, which predicts a much higher extinction coefficient. This can be caused by errors in the cell size characterization via AutoCell, given that, for cell sizes under 200 μm the paint can penetrate into the cells and, thus, the software measurements can yield lower values than the real ones [27]. A higher value of the extinction coefficient is found, as expected, in the FTIR method in comparison with the subtraction method, given that no integrating sphere was used and, therefore, almost 96% of the scattered radiation was lost. In spite of that, the same tendency $K_{MD} > K_{TD} > K_Z$ is found in both materials and with the three methods.

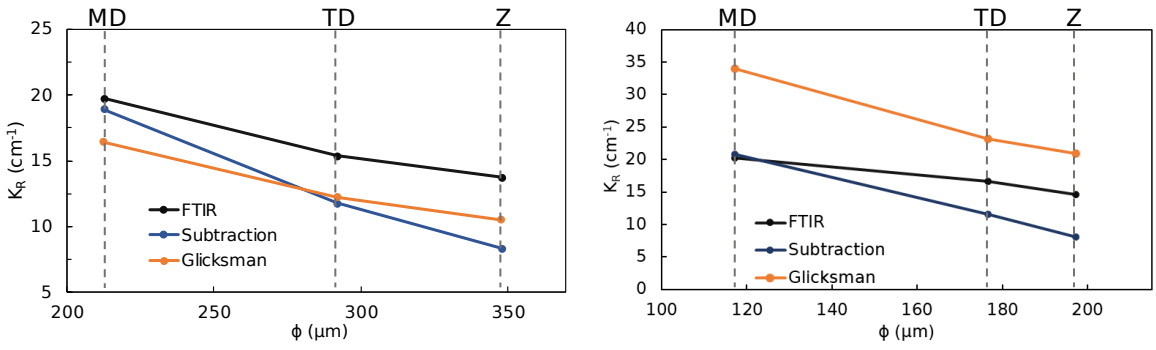

Figure 15. Summary of the results of K_R obtained by all methods for the samples BXPS1 (left), and BXPS2 (right).

Gathering all the results of the regressions of the ratios extinction coefficients with ratios of cell size (Figure **16**), one can see that there is good agreement between the

FTIR and Glicksman methods. Interestingly, a greater dependence of the ratios of K_R with the ratios of cell sizes is found with the subtraction method.

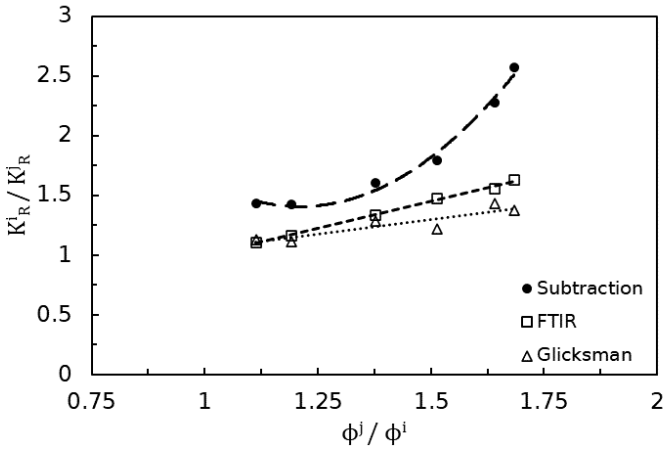

Figure 16. Summary of the results of the regressions of the ratios of extinction coefficients in two different directions and the inverse ratio of their respective cell sizes in all methods for the samples BXPS1 and BXPS2.

- ***Radiative contribution λ_r to the total thermal conductivity.***

Once all the results of the Rosseland extinction coefficient are obtained, the radiative contribution can be computed. Figure **17** shows the values of λ_r for the first set of materials obtained by all the methods previously seen. The overall tendency matches the expected: an increase in the radiative contribution as cell size grows. For both samples, the contributions yielded by each principal direction are clearly distinguishable, which proves the existence of different radiative transfer behaviours in each direction. It can be observed that, for both materials, the FTIR and Glicksman methods predict a decrease in the radiative contribution of approximately 1 $mW/(m\,K)$ when reorienting the material from the Z direction to the MD direction. This difference would represent a 20% of the original radiative contribution. On the other hand, the subtraction method predicts a decrease of about 4.5 $mW/(m\,K)$, which would represent a 50% of the original contribution. In any case, this is a remarkable fact, given that these materials are typically applied in the Z direction and are used for many years. Using the materials in the direction in which the cell size is smaller (MD direction) can undoubtedly be a significant energy saving.

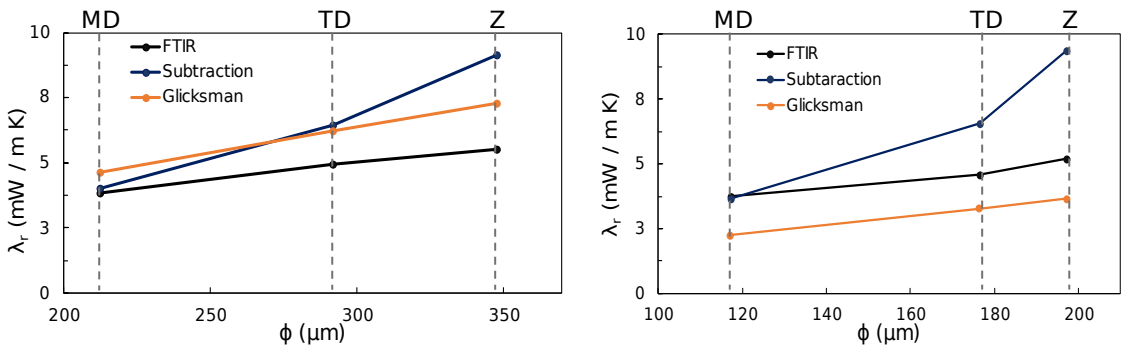

Figure 17. Summary of the results of λ_r obtained by all methods for the samples BXPS1 (left), and BXPS2 (right).

- ***All contributions of the heat transfer mechanism.***

Figure **18** shows an example of the dependence of the different contributions obtained using the subtraction method with cell size for the samples BXPS1 and BXPS2. Under the hypothesis of the theoretical equations (4) and (6), it seems appropriate to claim that the only mechanism significantly dependent of cell size is the radiative one, i.e., the differences between planes are only due to the different radiation contributions. Comparing between materials, one can see that the contribution of conduction through the gas phase are similar in both materials, while the one in the solid is not, due to the higher relative density of the BXPS2 material.

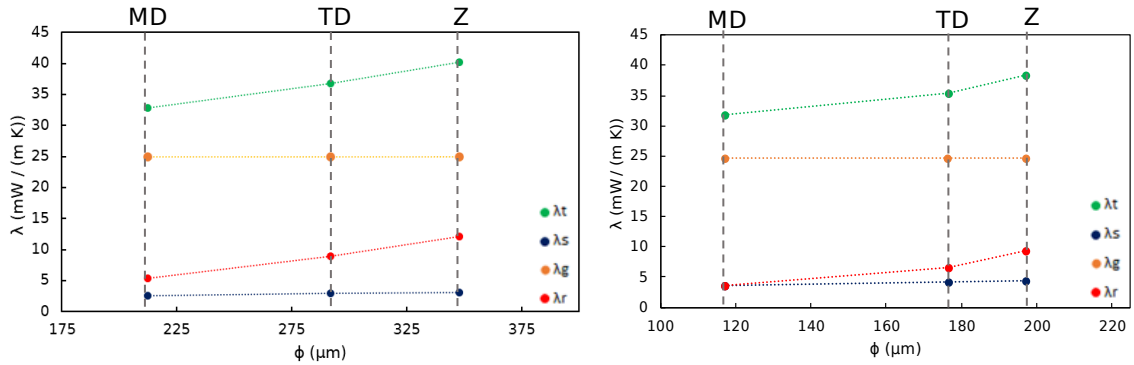

Figure 18. Dependence of the different contributions and the total conductivity with cell size in the case of BXPS1 (left) and BXPS2 (right) at a mean temperature between the Laser Comp's plates of 20 ^{o}C.

It is also interesting to evaluate the weight of each heat transfer mechanisms. It can be observed (see Figure **19**) that the mechanism of conduction through the gas accounts for about $60-75\%$ of the total conductivity in both cases. However, the solid conduction does it only for about $6-11\%$, leaving the radiative transfer mechanism a contribution of around $15-30\%$ in BXPS1 and $10-25\%$ in BXPS2.

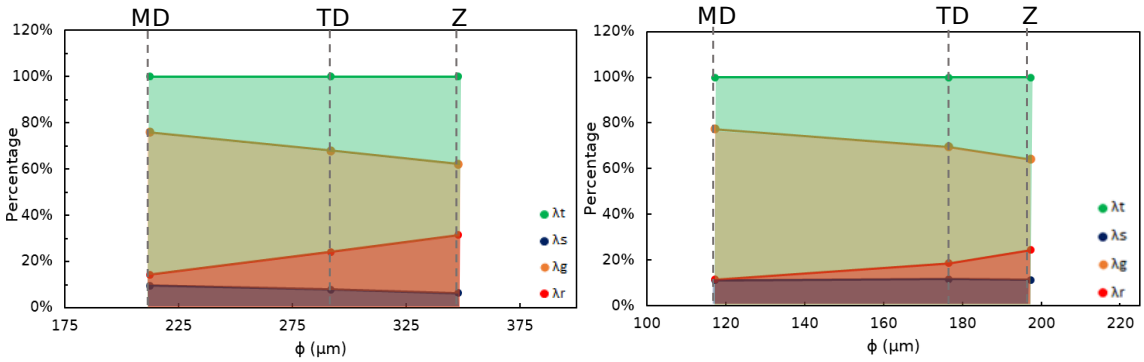

Figure 19. Dependence of the percentage of all contributions to the total conductivity with cell size in the case of BXPS1 (left) and BXPS2 (right) at a mean temperature between the Laser Comp's plates of 20 ^{o}C.

4.1 Second set of materials.

- ***Structural characterization.***

A structural characterization was carried out for the materials in the second set. The results are gathered in Table 7, where the samples were sorted from lowest to highest mean cell size. As already commented before, the value of f_s was set to be the constant value of 0.18. Similar to the samples in the first set, the pattern $\phi^Z > \phi^{TD} > \phi^{MD}$ is found. The anisotropy ratios take values in a wide range $(0.8 - 1.2)$. These foams are less anisotropic than the ones analysed in the first set.

Table 7. Results of the main cellular structural parameters of the second set of materials.

Sample	$\phi_Z(\mu m)$	$\phi_{TD}(\mu m)$	$\phi_{MD}(\mu m)$	R_Z	R_{TD}	R_{MD}	f_s
YXPS0	60	59	57	1.0	1.0	1.0	0.18
YXPS1	123	118	104	1.11	1.04	0.86	0.18
YXPS2	165	148	146	1.12	0.95	0.93	0.18
YXPS3	182	167	141	1.18	1.03	0.81	0.18
YXPS4	202	185	154	1.19	1.04	0.80	0.18
YXPS5	284	254	221	1.20	1.01	0.82	0.18

- ***Thermal characterization.***

The total conductivities of all samples in the second set at a mean temperature of the plates of $20ºC$ are shown in Figure 20. In contrast with the results of the first set, a clear difference in the tendency between the principal directions is not found. This is probably due to the imprecision of the adaptation of the thermal conductivity measurement for small samples (see Figure 8). The accuracy of this measurement is lower than that when using larger samples and, due to this, the differences between samples cannot be clearly detected. Therefore, it should also not be expected to find a good tendency of the values of K_R obtained out of these total thermal conductivity data. Despite that, the overall results reveal a nearly constant dependence of λ_T with ϕ and, taking a look at the mean values (green line) this statement seems to be reinforced.

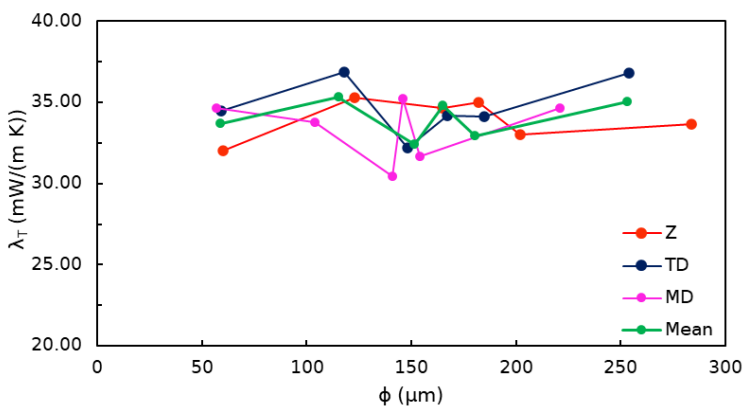

Figure 20. Total conductivity λ_T of the second set of materials when the mean temperature of the plates of the Laser Comp is 20 $ºC$. A distinction between the principal directions in which the temperature gradient is pointing in each case is made.

- ***Extinction coefficient.***

The results of the Rosseland extinction coefficient using the three methodologies outlined in section 3.2 are shown here for the case of the second set of materials.

I) FTIR spectroscopy method.

Similar to the case of the first set, the behaviour in the three principal directions is clearly distinguishable (see Figure (**21**)). However, the tendency of the second set of materials is different. One would expect lower extinction coefficients as cell size grows, but, instead, a maximum is observed near 150 μm for each material direction, as already found by Placido *et al.* [9]. This maximum represents a transition between two different scattering mechanisms. Above 150 μm, the Mie scattering takes places, giving a decreasing dependence of K_R with ϕ. Below 150 μm, the Rayleigh scattering appears, which only occurs when the radiation finds scattering points of lower size than $1/10$ times the wavelength of that radiation and predicts the inverse relation to the Mie scattering. In this case, given that the lowest wavenumber used in the FTIR experiment is 600 cm^{-1}, the maximum scattering points size for the Rayleigh scattering to appear would be approximately 1.7 μm, which can be the thickness of a perceptible amount of cell walls. It is remarkable that a clear difference in the extinction coefficients of the three principal directions is observable, in fact, this is $K_{MD} > K_{TD} > K_Z$, in agreement with the results for the first set and with the trend for the cell sizes in these materials.

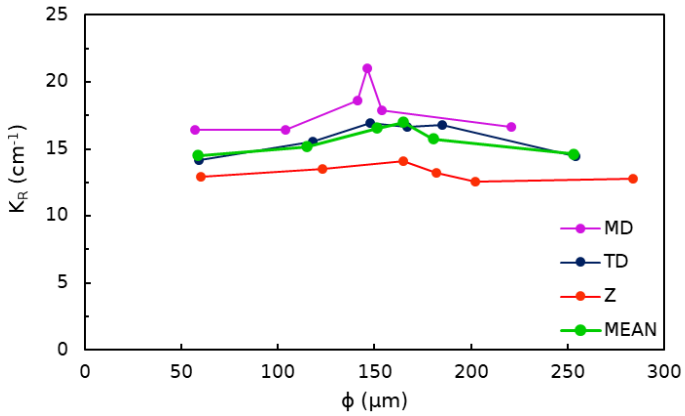

Figure 21. Dependence of K_R with the cell size for the second set of materials in Table **1** with the FTIR method.

II) Method of subtraction of contributions from the total conductivity.

As already stated before, the tendency of K_R obtained by this method should not be expected to be logical, due to the experimental error in the measurement of the thermal conductivity. The results are shown in Figure **22**. It is interesting to see that, looking at

the mean values line (green line) a maximum appears near 150 μm, similar to the one obtained with the FTIR method.

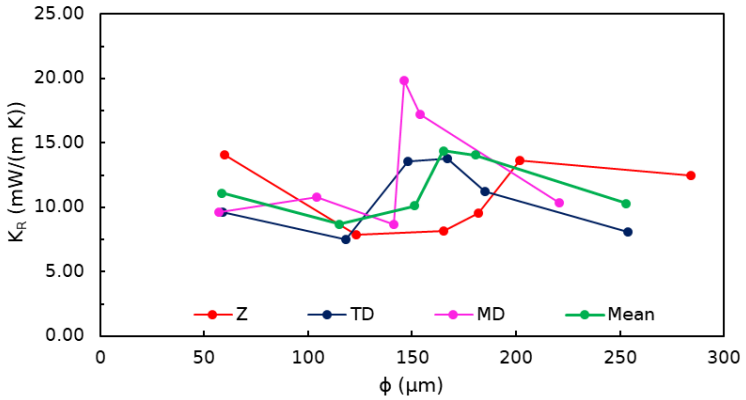

Figure 22. Dependence of K_R with the cell size for the second set of materials with the subtraction method.

III) Glicksman's model method.

Applying Equation (8) with the characteristics of the materials exposed in Table **7**, the results shown in Figure **23** are obtained. Interestingly, the Glicksman model predicts a decreasing dependence of K_R with the increase in cell size but, more specifically, for sizes above 150 μm this dependence tends to almost a constant value. Given that Glicksman based his theory in the Mie scattering region, a bad accuracy should be expected for cell sizes below 150 μm. As expected, almost no change in K_R is found for the first points, which represent the samples with no anisotropy. As the cell size grows, there is anisotropy and the difference between planes becomes larger.

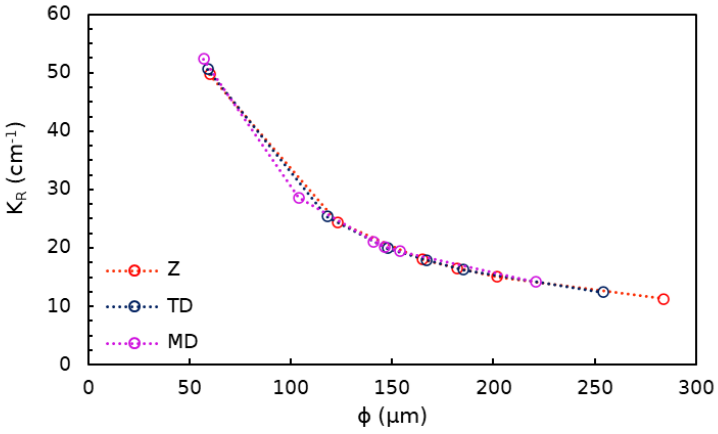

Figure 23. Dependence of K_R with the cell size for the second set of materials in Table **1** with the Glicksman model method.

- ***Comparison between the FTIR and Glicksman methods.***

Ignoring the results from the subtraction method because of its lack of accuracy, it can be seen in Figure **24** that there is a good agreement between the FTIR and the

Glicksman methods, at least for cell size over 150 μm,where the Mie scattering takes places. Even though a clear difference between principal directions is found in the FTIR method, it is not the case for the Glicksman model. This problem could be solved measuring the fractions of mass in the struts f_s for all the samples in this set with X-ray tomography. If a range of different f_s with a logic dependence with cell size was found, the predictions of the Glicksman model could be improved.

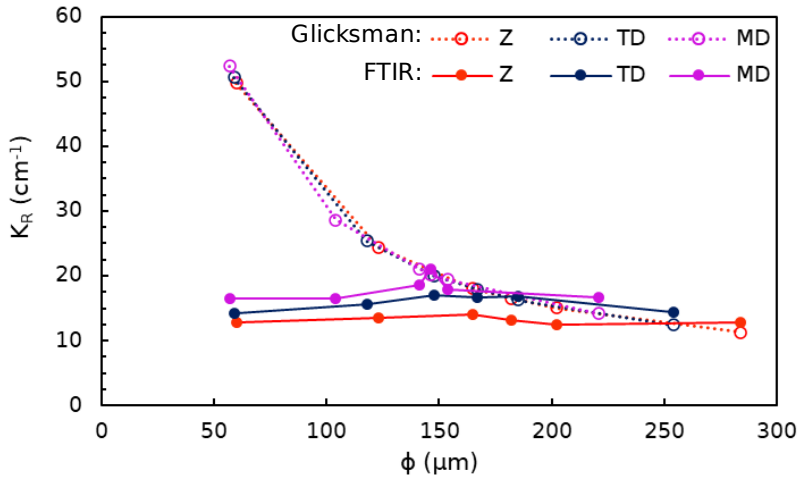

Figure 24. Summary of the results of K_R obtained by the FTIR and Glicksman methods for the samples in the second set.

- ***Radiative contribution λ_r to the total thermal conductivity.***

Again, ignoring the results from the subtraction method, the results of the radiative contribution to the total thermal conductivity found with the FTIR and Glicksman methods are found in Figure **25**. Similar to the extinction coefficient, the tendency in both methods seems to be similar for cell sizes above 150 μm. The FTIR experiments predict a decrease of about 1.4 $mW/(m\ K)$ when reorienting the materials from the Z direction to the MD direction. To this respect, Glicksman predicts a decrease of about 1.4 $mW/(m\ K)$ for the samples with highest anisotropy and almost no difference for the isotropic samples, as expected. For those samples with a major change in the radiative contribution, it is remarkable that it can represent up to almost 35% of the original contribution. This information, if used properly, can lead to a significant energy saving if the material has a long-term insulating application.

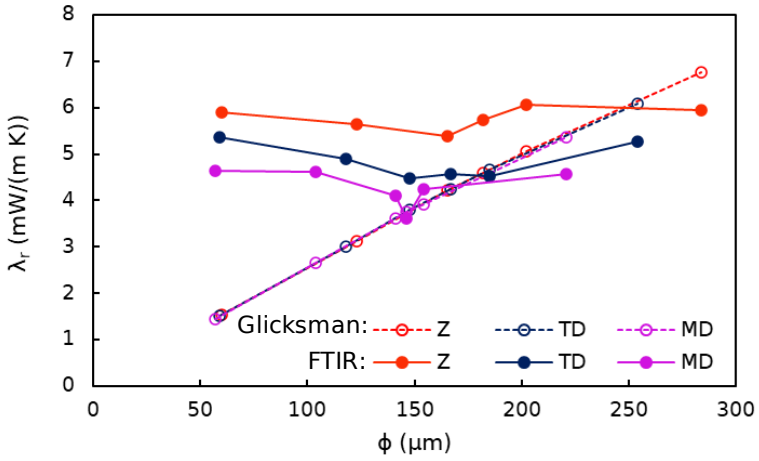

Figure 25. Summary of the results of λ_r obtained by the FTIR and Glicksman methods for the samples in the second set.

- ***All contributions of the heat transfer mechanism.***

Figure **26** shows the different contributions to the total thermal conductivity in a YXPS0 and a YXPS5 sample. In this case, instead of obtaining the radiative contribution subtracting terms from the total conductivity, given that the gathered values of λ_T are not reliable, the total conductivity was obtained by using the results of the FTIR radiative contribution, summing the λ_s and λ_g terms to the radiative contribution λ_r obtained from the FTIR method to get λ_T. The results show, as expected, very little dependence of all contributions with the cell size (i.e., with the plane of measurement), given that, as found before, the maximum achievable difference in the radiative contribution between planes is only 1.4 $mW/(m\,K)$ in both cases, and the solid and gas conduction contributions are almost constant with cell size. Therefore, in these samples with lower anisotropies, the differences in thermal properties between planes are smaller.

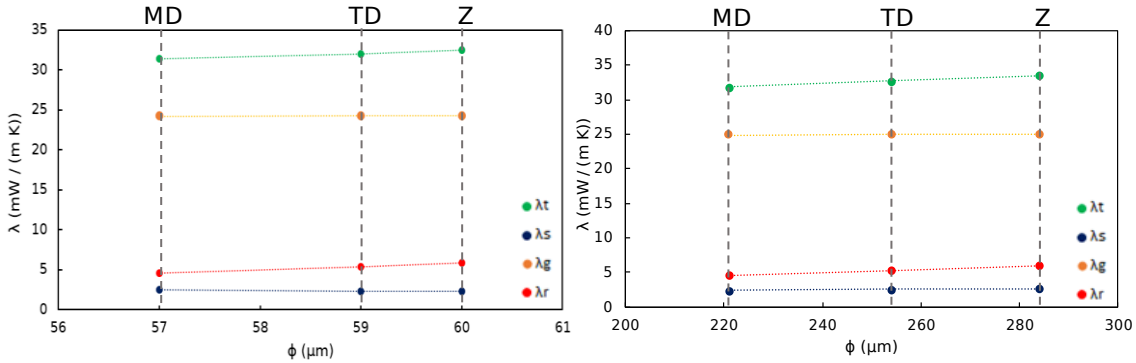

Figure 26. Dependence of the different contributions and the total conductivity with cell size in the case of YXPS0 (left) and YXPS5 (right) at a mean temperature of 20 ºC.

Regarding the contribution's percentages, which are shown in Figure **27**, it can be seen that, again, the gas conduction is the most contributing one, with about $75-80\%$ over the total. The solid conduction and the radiative transfer contributions account for about $7-8\%$ and $15-18\%$ respectively in both materials.

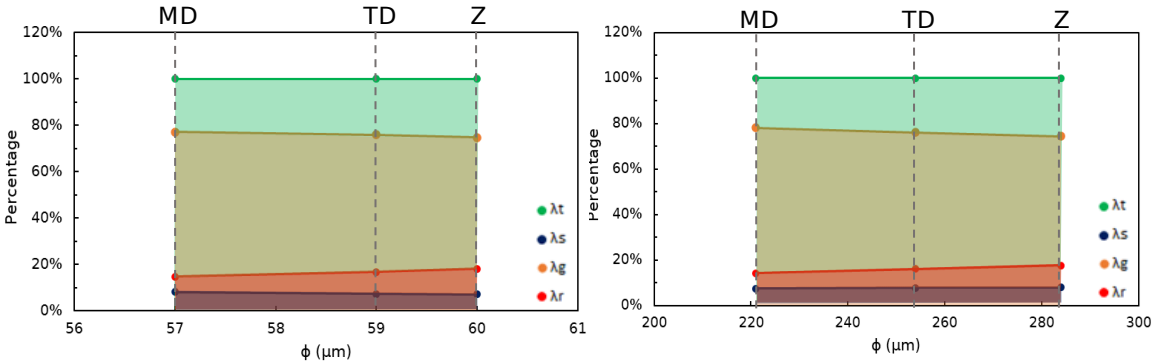

Figure 27. Dependence of the percentage of all contributions to the total conductivity with cell size in the case of YXPS0 (left) and YXPS5 (right) at a mean temperature between the Laser Comp's plates of 20 ºC.

5. Conclusions and future work

5.1 Conclusions.

Three different methodologies were used to calculate the Rosseland extinction coefficient and, with that, the radiative transfer contribution to the total thermal conductivity. These methodologies are FTIR spectroscopy, derivation from the total conductivity via subtraction of the other contributions, and the theoretical model proposed by Glicksman. First, two different sets of materials were characterized. The first set, which is composed of two XPS foams of medium density, was found to have a high anisotropic character, with values of the ratio of anisotropy ranging from about 0.6 in the MD direction to almost 1.4 in the Z direction. Both materials in this set share the same cell size tendency $\phi_Z > \phi_{TD} > \phi_{MD}$. Regarding the total thermal conductivity, a clear difference between the results in the three directions was found, being the MD direction the one with the lowest values and Z the one with the highest ones. The second set, which is composed of six XPS foams of low and similar densities, was found to have the same cell size tendency and lower anisotropy ratios, ranging, in this case, from 0.8 in the MD direction to 1.2 in the Z direction. The total conductivity showed a constant dependence with cell size.

Looking at the results yielded by the three methodologies, it seems clear that there are noticeable differences in the contribution of the radiative transfer mechanism to the total thermal conductivity in each principal direction of the cellular materials under study. In fact, all methodologies predict the same trends for the first set of samples. This is proved to be caused by their anisotropic nature. In fact, the greater the cell size is in one direction, the greater the radiative contribution is in that direction. In fact, we have proved that thermal conductivity by radiation is larger in Z direction, followed by TD and MD direction. This can affect significantly the performance of polymeric cellular materials in their applications as heat insulators, given that, in very anisotropic materials, the values of the total conductivity in each direction may vary considerably due to this behaviour of the radiative transfer. In fact, reorienting the materials from the Z direction to the MD direction may lead to a decrease of up to 10 $mW/(m\,K)$ (firs set of samples at high temperatures), in the total conductivity, which represents a difference

of about a 20% with respect to the original. Given that these materials are used for dozens of years, this can end up being a considerable energy saving.

Interestingly, looking at the results of the FTIR spectroscopy of the second set, a minimum in the radiative contribution is found around 150 μm. Above that value, the results show the expected dependence with cell size and are well predicted by the Glicksman model. Below that threshold the behaviour is totally different, and the model cannot predict the experimental data. This is explained by a transition in the scattering mechanism that takes places. For cell sizes lower than 150 μm that mechanism changes from Mie to Rayleigh scattering.

Regarding FTIR spectroscopy and the subtraction methodologies, the overall results show similar tendencies of the dependence of the radiative contribution with cell size. Also, one can see that there is a good agreement between the results derived from these experimental measurements and the results calculated using the Glicksman's theoretical model in the first set of materials. This is not the case for the second set, in which the montage adaptation to measure the total thermal conductivity results to be imprecise, and then, the extinction coefficient calculated using the subtraction method are also inaccurate and the transition between the Mie and Rayleigh scatterings is observed, leading to the Glicksman model yielding inaccurate results for samples with cell sizes lower than 150 μm.

5.2 Future work.

The results obtained have shown very interesting trends in a topic not analysed in detail before and, in fact, the research could continue in different directions, which are outlined below:

i) Using an integrating sphere to perform more accurate measurements of the extinction coefficient using the FTIR spectroscopy method. The use of this device will help to recapture and measure all the radiation scattered by the samples, which in other case would not reach the detector.

ii) Measuring the total thermal conductivity of the samples in the second set with a higher accuracy. This will allow to obtain more reliable trends for the radiation contribution in this set of samples using the subtraction method.

iii) Analysing experimentally and theoretically the maximum found for the extinction coefficient in the second set of samples in more detail, stablishing a stronger knowledge basis on the transition between the Rayleigh and Mie scatterings.

6. References

[1] AEE., *The European environment: state and outlook 2020: knowledge for transition to a sustainable Europe.* LU: Publications Office, 2019. Accessed: May 21, 2022. [Online]. Available: https://data.europa.eu/doi/10.2800/96749

[2] M. Arduini, J. Manara, and C. Vo, “Modeling of Radiative Properties of Polystyrene Foams Containing IR-Opacifiers,” *Cellular Polymers*, vol. 35, no. 2, pp. 49–66, Mar. 2016, doi: 10.1177/026248931603500201.

[3] C. V. Vo, F. Bunge, J. Duffy, and L. Hood, “Advances in Thermal Insulation of Extruded Polystyrene Foams,” *Cellular Polymers*, vol. 30, no. 3, pp. 137–156, May 2011, doi: 10.1177/026248931103000303.

[4] C. Sáiz Arroyo, “Fabricación de materiales celulares mejorados basados en Poliolefinas. Relación procesado-composición-estructura-propiedades,” Universidad de Valladolid, 2012. doi: 10.35376/10324/1759.

[5] D. Eaves, Ed., *Handbook of polymer foams*. Shawbury, Shrewsbury, Shropshire, U.K: Rapra Technology, 2004.

[6] P. G. Collishaw and J. R. G. Evans, “An assessment of expressions for the apparent thermal conductivity of cellular materials,” vol. 29, no. 2, pp. 486–498, 1994, doi: doi:10.1007/bf01162512.

[7] R. A. Campo-Arnáiz, M. A. Rodríguez-Pérez, B. Calvo, and J. A. de Saja, “Extinction coefficient of polyolefin foams: Extinction Coefficient of Polyolefin Foams,” *J. Polym. Sci. B Polym. Phys.*, vol. 43, no. 13, pp. 1608–1617, Jul. 2005, doi: 10.1002/polb.20435.

[8] N. C. Hilyard and A. Cunningham, Eds., *Low density cellular plastics: Physical basis of behaviour*. Dordrecht: Springer Netherlands, 1994. doi: 10.1007/978-94-011-1256-7.

[9] E. Placido, M. C. Arduini-Schuster, and J. Kuhn, “Thermal properties predictive model for insulating foams,” *Infrared Physics & Technology*, vol. 46, no. 3, pp. 219–231, Jan. 2005, doi: 10.1016/j.infrared.2004.04.001.

[10] D. Doermann and J. F. Sacadura, “Heat Transfer in Open Cell Foam Insulation,” *Journal of Heat Transfer*, vol. 118, no. 1, pp. 88–93, Feb. 1996, doi: 10.1115/1.2824072.

[11] M. Arduini-Schuster, J. Manara, and C. Vo, “Experimental characterization and theoretical modeling of the infrared-optical properties and the thermal conductivity of foams,” *International Journal of Thermal Sciences*, vol. 98, pp. 156–164, Dec. 2015, doi: 10.1016/j.ijthermalsci.2015.07.015.

[12] A. Biedermann *et al.*, “Analysis of Heat Transfer Mechanisms in Polyurethane Rigid Foam,” *Journal of Cellular Plastics*, vol. 37, no. 6, pp. 467–483, Nov. 2001, doi: 10.1106/KEMU-LH63-V9H2-KFA3.

[13] N. C. Balaji, M. Mani, and B. V. V. Reddy, “Discerning Heat Transfer in Building Materials,” *Energy Procedia*, vol. 54, pp. 654–668, 2014, doi: 10.1016/j.egypro.2014.07.307.

[14] C. Rémi, B. Dominique, and Q. Daniel, “Radiative Properties of Expanded Polystyrene Foams,” *Journal of Heat Transfer*, vol. 131, no. 1, p. 012702, Jan. 2009, doi: 10.1115/1.2994764.

[15] A. Kaemmerlen, C. Vo, F. Asllanaj, G. Jeandel, and D. Baillis, “Radiative properties of extruded polystyrene foams: Predictive model and experimental results,”

Journal of Quantitative Spectroscopy and Radiative Transfer, vol. 111, no. 6, pp. 865–877, Apr. 2010, doi: 10.1016/j.jqsrt.2009.11.018.

[16] A. Öchsner, G. E. Murch, and M. J. S. deLemos, *Cellular and Porous Materials: Thermal Properties, Simulation and Prediction*. WILEY-VCH, 2008.

[17] M. A. Schuetz and L. R. Glicksman, "A Basic Study of Heat Transfer Through Foam Insulation," *Journal of Cellular Plastics*, vol. 20, no. 2, pp. 114–121, Mar. 1984, doi: 10.1177/0021955X8402000203.

[18] R. J. J. Williams and C. M. Aldao, "Thermal conductivity of plastic foams," *Polym. Eng. Sci.*, vol. 23, no. 6, pp. 293–298, Apr. 1983, doi: 10.1002/pen.760230602.

[19] J. Kuhn, H.-P. Ebert, M. C. Arduini-Schuster, D. Büttner, and J. Fricke, "Thermal transport in polystyrene and polyurethane foam insulations," *International Journal of Heat and Mass Transfer*, vol. 35, no. 7, pp. 1795–1801, Jul. 1992, doi: 10.1016/0017-9310(92)90150-Q.

[20] R. Caps, U. Heinemann, J. Fricke, and K. Keller, "Thermal conductivity of polyimide foams," *International Journal of Heat and Mass Transfer*, vol. 40, no. 2, pp. 269–280, Jan. 1997, doi: 10.1016/0017-9310(96)00134-2.

[21] C. Tseng and K. Kuo, "Thermal radiative properties of phenolic foam insulation," *Journal of Quantitative Spectroscopy and Radiative Transfer*, vol. 72, no. 4, pp. 349–359, Feb. 2002, doi: 10.1016/S0022-4073(01)00129-7.

[22] S. M. Pascual, M. Á. R. Pérez, and C. S. Arroyo, "Desarrollo de nuevos agentes espumantes endotérmicos para la fabricación de materiales celulares poliméricos," p. 83.

[23] "Frontmatter," in *Heat Conduction*, Hoboken, NJ, USA: John Wiley & Sons, Inc., 2012, pp. i–xxx. doi: 10.1002/9781118411285.fmatter.

[24] A. P. Boresi and R. J. Schmidt, *Advanced mechanics of materials*, 6. ed. New York: Wiley, 2003.

[25] V. Bernardo, J. Martin-de Leon, and M. A. Rodriguez-Perez, "Anisotropy in nanocellular polymers promoted by the addition of needle-like sepiolites," *Polym. Int.*, vol. 68, no. 6, pp. 1204–1214, Jun. 2019, doi: 10.1002/pi.5813.

[26] J. P. Holman, *Heat Transfer*, 10th ed. New York, NY: McGraw-Hill, 2010.

[27] J. Torre Ordás, "Desarrollo de una metodología basada en microscopía óptica para la caracterización de la estructura celular de materiales celulares," *UVaDOC*, 2021.

[28] B. K. Sharma, *Industrial Chemistry*, 15th ed. Meerut: GOEL Publishing House, 2006.

[29] M.-T. I. I. all rights reserved, "Measuring Density with Laboratory Balance." https://www.mt.com/ch/en/home/applications/Laboratory_weighing/density-measurement.html (accessed Jun. 18, 2022).

[30] "CellMat Technologies – Software and methodology for the characterization of cellular structures." http://www.cellmattechnologies.com/en/software-and-methodology-for-the-characterization-of-cellular-structures/ (accessed Jun. 05, 2022).

[31]Schindelin, J., Rueden, C. T., Hiner, M. C., & Eliceiri, K. W. (2015)., *ImageJ*. [Online]. Available: The ImageJ ecosystem: An open platform for biomedical image analysis. Molecular Reproduction and Development,82(7–8), 518–529.doi:10.1002/mrd.22489

[32S. Pérez-Tamarit, E. Solórzano, A. Hilger, I. Manke, and M. A. Rodríguez-Pérez, "Multi-scale tomographic analysis of polymeric foams: A detailed study of the cellular structure," *European Polymer Journal*, vol. 109, pp. 169–178, Dec. 2018, doi: 10.1016/j.eurpolymj.2018.09.047.

[33]M. Tasumi, "Introduction to Experimental Infrared Spectroscopy," p. 404.

[34]J. R. Howell, M. P. Mengüç, and R. Siegel, *Thermal radiation heat transfer*, Sixth edition. Boca Raton, Fla. London New York: CRC Press, Taylor & Francis Group, 2016.

[35]F. Kreith, M. Raj M., and B. Mark S., *Principios de transferencia de calor*. CengageLearning, 2011.

[36]"Standard Test Method for Steady-State Thermal Transmission Properties by Means of the Heat Flow Meter Apparatus." https://www.astm.org/c0518-21.html (accessed May 29, 2022).

[37]"Air - Thermal Conductivity vs. Temperature and Pressure." https://www.engineeringtoolbox.com/air-properties-viscosity-conductivity-heat-capacity-d_1509.html (accessed Jun. 07, 2022).